DEEP-LEVEL DEFECTS IN SEMICONDUCTORS: STUDIES BY MAGNETIC RESONANCE

Contents:

By:
C.A.J.Ammerlaan
Natuurkundig Laboratorium, Universiteit van Amsterdam,
Valckenierstraat 65, 1018 XE Amsterdam, The Netherlands.

Summary of lectures presented at the
Summer School on Semiconductor Physics
January 31 - February 11, 1983
Universidade Estadual de Campinas, Campinas, S.P., Brasil.

1. Introduction

1a. Paramagnetic centers in semiconductors

In semiconductors which are both perfectly ordered and pure, all spins and orbital momenta are paired off. These materials are diamagnetic and provide no signals in magnetic resonance. Paramagnetism can arise from lattice defects and impurities in these crystals /1,2/.The following cases can be distinguished:

- Surface states. Unpaired electrons will reside in dangling bonds at the semiconductor surface. The density of these states is reduced by bond reconstruction, by which new surface bonds are formed which are lower in energy and are doubly occupied. The surface resonance is a broad structureless isotropic line with g-value $g = 2.0055$. The density of centers can be influenced by surface treatment, for instance sandblasting increases while chemical etching reduces the number of surface states /3-5/.
- Dislocations. Several resonances associated with dislocations are known. Broken bonds in the dislocation core may contain electrons with non-paired spin. Paramagnetism may also arise from impurities precipitated onto the dislocation (decoration) or from defects created by dislocation motion. Dislocations can be introduced in a controlled manner by plastic deformation at elevated temperature, typically $600 - 800^{o}C$ in the case of silicon /6/.
- Free carriers. In highly doped semiconductors free electrons will be excited into conduction band states, or holes in upper valence band states in p-type material, giving rise to Pauli spin paramagnetism. The g-value for electrons in the silicon conduction band is $g = 1.99875$. Resonances from free holes have not yet been reported /3,7-9/.
- Point crystal lattice defects, and small aggregates of these defects. Typical examples in this category are the monovacancy, divacancy and multivacancies. They are created by quenching of samples, or in a more controlled manner by particle irradiation, in particular by electron irradiation /10/.
- Impurities, which are atoms of a different chemical nature than the host. This important class includes the shallow dopants, consisting of the group V donors in silicon and germanium: P, As, Sb, /3,11-14/ and the group III acceptors: B, Al, Ga, In /11,15/. Several other impurities are known to introduce levels which are deep in the bandgap. The impurities S /16/ and N /17,18/ are examples of impurities occupying substitutional sites in the lattice, while transition metals (Fe,Cu) preferentially are found on interstitial sites. Small impurity complexes, such as the iron-acceptor pairs, are also often paramagnetic /19,20/.
- Associates between lattice defects and impurities. Mobile defects can

be trapped at other defects forming complexes, or even larger clusters. Well-studied examples are the oxygen-vacancy /21/ and the phosphorus-vacancy /22/ centers.

- Structural defects. In compound semiconductors a constituent atom may occupy a position on the wrong sublattice. This can be the result of non-stoichiometric composition or of other specific treatments (irradiation, dislocation motion). These are called antisite defects /23/.

All of these defects introduce electron energy levels in the bandgap. Therefore, their charge state and hence their paramagnetism can be affected by the Fermi level, whether in equilibrium or non-equilibrium conditions. Doping and ionization (e.g. by illumination) are tools to enhance the paramagnetic state.

1b. Principles of magnetic resonance

The energy of an electron, with magnetic moment $\vec{\mu}$, when placed in a magnetic field $\vec{B}$ will change by an amount $-\vec{\mu}.\vec{B}$. This is the familiar Zeeman effect. The magnetic moment is related to the angular momentum $\vec{J}$ by the proportionality $\vec{\mu} = g\mu_B\vec{J}$, with μ_B the Bohr magneton and g the spectroscopic splitting factor. For orbital motion $g = 1$ and for pure spin $g = 2$, more exactly $g = 2.0023$. In the general case of coupled orbital and spin momentum the g-factor is given by the Landé formula. In a magnetic field the quantized sublevels, labelled by m_J, will split in energy. This is illustrated in figure 1.

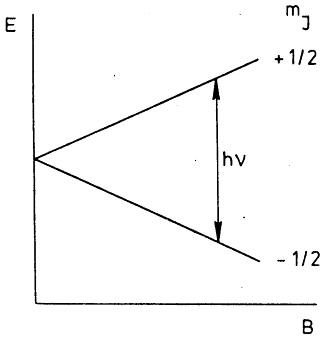

Figure 1. The Zeeman splitting of energy levels for $J = 1/2$ as a function of the magnetic field B.

Transitions between the sublevels can be induced by electromagnetic radiation. This phenomenon is electron paramagnetic resonance, EPR/24-26/. Stimulated absorption and emission will occur when the quantum of radiation $h\nu$ equals the energy separation of two levels. The former process is usually stronger as in thermodynamic equilibrium the lower level is (slightly) more populated. The resonance condition for magnetic dipole transitions, with selection rule $\Delta m_J = 1$, is given by

$$h\nu = g\mu_B B. \qquad (1)$$

In the usual experimental situation the spectrometer is designed for a microwave frequency which is only slightly variable and the resonance condition is satisfied by adjusting the magnetic field. The classical spectrometer is operated in the X-band at $\nu \approx 9 \times 10^9$ Hz. For $g = 2$ the resonance then occurs at $B \approx 0.32$ T.

Nuclear magnetic resonance (NMR) is the equivalent experiment applied to magnetic nuclei, $I \neq 0$, rather than to electrons. The resonance condition is similarly

$$h\nu = g_N\mu_N B. \qquad (2)$$

Since the nuclear moments $-g_N\mu_N\vec{I}$ are typically 3 orders of magnitude smaller than those of electrons, the energy splittings are correspondingly smaller. Resonance frequencies are in the 1 - 10 MHz range for the magnetic fields of about 1 T which are usually employed.

Both resonance techniques can be combined to great advantage in what is called electron-nuclear double resonance (ENDOR) /27/. A level scheme for a system with electron spin $J = \frac{1}{2}$ and nuclear spin $I = \frac{1}{2}$ is shown in figure 2. The energy levels are at:

$$E = g\mu_B B m_J - g_N\mu_N B m_I. \qquad (3)$$

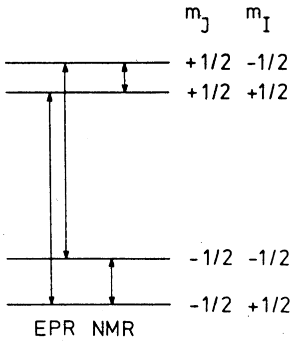

Figure 2. Energy levels for a J = 1/2, I = 1/2 spin system, with EPR and NMR transitions indicated.

The EPR transitions are characterized by $\Delta m_J = 1, \Delta m_I = 0$, while in NMR only the nuclear quantum number changes by one. In ENDOR an EPR is induced with high microwave power, destroying the thermal distribution according to Boltzmann statistics over the two states involved by saturating the transition. If under such conditions an NMR transition is induced it will be observable in the EPR by a change in intensity of the latter signal. NMR is characterized by high energy resolution, typically 10^3 times better than in EPR. However, EPR surpasses NMR by its superior sensitivity, which is in the order of 10^6 times better. The attraction of ENDOR is that it combines both advantages to a large extent.

1c. Spin-Hamiltonian

A very useful concept introduced to analyse and acting as an intermediate step in understanding magnetic resonance results is the spin-Hamiltonian /28-30 /. It is an expression which includes all relevant contributions to the energy dependent on the electron spin $\vec{J}$ and nuclear spin(s) $\vec{I}$. An effective spin value J is introduced by equating the number of electronic levels which in the ground state are required to describe the interactions properly, to 2 J + 1. The spin-Hamiltonian operator has a form like:

$$\begin{aligned} H = \; & \mu_B \vec{B}.\overleftrightarrow{g}.\vec{J} + \vec{J}.\overleftrightarrow{D}.\vec{J} + a(J_x^4 + J_y^4 + J_z^4) + \dots \\ & - g_N \mu_N \vec{B}.\vec{I} + \vec{I}.\overleftrightarrow{Q}.\vec{I} + \dots \\ & + \vec{J}.\overleftrightarrow{A}.\vec{I} + \dots \end{aligned} \qquad (4)$$

The first line enumerates some interactions in which electrons are involved only: the Zeeman energy, a zero-field term, and the cubic field energy, respectively. In the second line some energy terms associated with one nucleus of spin I are given: its Zeeman and quadrupole energy. An interaction term between electrons and nucleus, called hyperfine interaction, is given on the third line. Depending on the complexity of the system a different number of terms is required for a satisfactory description of results. The larger the number of spins involved and the lower the symmetry, the more terms will be needed. The coupling parameters, such as $\overleftrightarrow{g}$, $\overleftrightarrow{D}$, $\overleftrightarrow{Q}$, $\overleftrightarrow{A}$, are generally tensors as they have to account for the angular dependent properties of coupled vector quantities. In the analysis of experimental results they are considered as adjustable parameters which are matched to obtain best agreement. Once their values are determined, they must be interpreted in more physical terms, i.e. in terms of atomic structure, interactions and wave functions. For g-tensors the theoretical means to do so are still in an unsatisfactory state. The interpretation of hyperfine interaction tensors is much more straightforward.

1d. g-Tensor

All paramagnetic centers, even the simplests, have an electronic g-value. This, therefore, is the most important spin-Hamiltonian parameter. Unfortunately a physical interpretation of the g-value, more generally g-tensor components, is difficult. In most cases the situation as regards orbital motion of defect electrons in crystals is very much different from that of free atoms. Strong crystalline fields with lower than cylindrical symmetry prevent circular orbital motion, leading to the phenomenon called quenching of orbital momenta. Therefore, there is spin-only paramagnetism with a corresponding g-value $g = 2.0023$. Small deviations from $g = 2.0023$ are caused by coupling of spin to the lattice through spin-orbit interaction. Only by this second order perturbation the presence of the crystal is represented in the g-value. The formal expression for the g-tensor components is /26,28/:

$$g_{\alpha\beta} = 2.0023\,\delta_{\alpha\beta} - 2\lambda \sum_{n\neq o} \frac{\langle 0|L_\alpha|n\rangle . \langle n|L_\beta|0\rangle}{E_n - E_o} \tag{5}$$

with $\alpha,\beta = x,y,z$. The spin-orbit coupling constant λ can be obtained from optical spectra. A calculation of $g_{\alpha\beta}$ requires knowledge of the ground and excited states $|0\rangle$ and $|n\rangle$ and of the excitation energies $E_n - E_o$. In the case of defects in covalent semiconductors this information is seldom available in sufficient detail. This represents an area where improvement should be achieved.

Without full quantitative understanding of the g-tensor components, the structure of the tensor still reflects the symmetry of the defect in the host crystal. Elemental semiconductors, such as silicon, crystallize in the diamond lattice. The symmetry, as seen from an atomic site, is specified by the point group $\bar{4}3m$. This point group contains 24 operations which leave the crystal invariant. Incorporation of a defect or impurity in the crystal may leave all these symmetry transformations intact, or may destroy some or all of them. A systematic analysis reveals that 8 different cases can be distinguished. These are cubic, tetragonal, rhombic I, rhombic II, trigonal, monoclinic I, monoclinic II and triclinic, in order of decreasing symmetry. Obviously, when a transformation (rotation, inversion, reflection) transforms a defect plus surrounding crystal into itself, then also the transformed g-tensor must be identical to the original. In mathematical terms, when the transformation is given by $\overleftrightarrow{R}$, then for a symmetry transformation $\overleftrightarrow{g} \equiv \overleftrightarrow{R}^{-1} . \overleftrightarrow{g} . \overleftrightarrow{R}$. This demonstrates that the existence of symmetry imposes constraints on the g-tensor. It may require some components to be equal, or to be zero. A specific structure of the g-tensor corresponds to each of the 8 symmetry cases mentioned. However, it is also possible that a symmetry transformation of the crystal transforms the defect into an orientation which is different from the starting configuration. The new defect orientation is related to the original one by the symmetry and its g-tensor is obtained from it by $\overleftrightarrow{g} = \overleftrightarrow{R}^{-1} . \overleftrightarrow{g} . \overleftrightarrow{R}$. The number of distinguishable defect orientations will be higher the lower the symmetry of the defect. It varies from 1 in the case of cubic symmetry to 24 for triclinic centers. Of course, since the g-tensors of the various orientations are related, the resonance fields as observed in EPR reflect this symmetry. For specific directions of the magnetic field the orientation of several defects may be equivalent, giving rise to coincidence of the resonance lines. This phenomenon is called orientational degeneracy. A one-to-one correspondence exists between the 8 cases of symmetry and the patterns of resonance fields of the variously oriented defects when the magnetic field is rotated in the $(0\bar{1}1)$-plane.

Some examples will illustrate these points. Figure 3 shows the g-factor of unionized phosphorus in silicon. A single impurity atom on a substitutional site has all symmetry operations with the lattice in common.

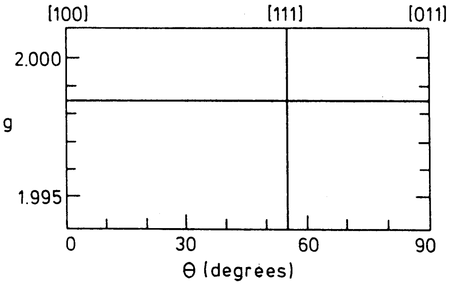

Figure 3. g-Value as a function of orientation of magnetic field for cubic symmetry, example phosphorus in silicon.

The g-tensor: $\begin{pmatrix} g_{xx} & 0 & 0 \\ 0 & g_{xx} & 0 \\ 0 & 0 & g_{xx} \end{pmatrix}$

reduces to a scalar g-value and the resonance field is isotropic. An intermediate case is exemplified by defects of trigonal symmetry, such as nitrogen in diamond (EPR spectrum: C-P1) and substitutional iron in silicon (EPR spectrum: Si-NL19). The structure of the g-tensor is

$$\overleftrightarrow{g} = \begin{pmatrix} g_{xx} & g_{xy} & g_{xy} \\ g_{xy} & g_{xx} & g_{xy} \\ g_{xy} & g_{xy} & g_{xx} \end{pmatrix} ,$$

containing two independent tensor components. Resonance patterns for $\overleftrightarrow{B}$ in the $(0\bar{1}1)$-plane are shown in figure 4. For $\vec{B}//[100]$ the orien-

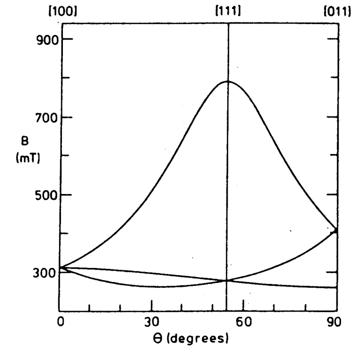

Figure 4. The resonance field B as a function of orientation of magnetic field for trigonal symmetry, example the spectrum Si-NL20 associated with an iron pair defect in silicon.

tational degeneracy is the maximal 4. Finally, the most general case is that of defects with lowest, i.e. triclinic symmetry. There are no constraints on the g-tensor which assumes the general form

$$\overleftrightarrow{g} = \begin{pmatrix} g_{xx} & g_{xy} & g_{zx} \\ g_{xy} & g_{yy} & g_{yz} \\ g_{zx} & g_{yz} & g_{zz} \end{pmatrix},$$

with all six components independent. The rotation pattern of resonance fields is illustrated by figure 5, representing the spectrum labelled

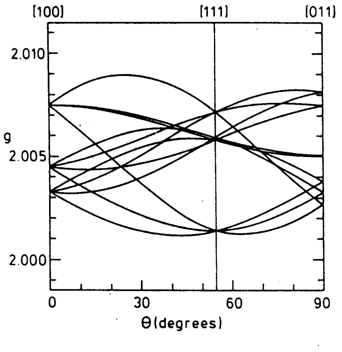

Figure 5. g-Values as a function of orientation of magnetic field for triclinic symmetry, example the spectrum Si-G10 associated with the neutral BV complex in silicon.

Si-G10, corresponding to the boron-vacancy complex in silicon. Examples illustrating the other cases also exist. These symmetry considerations are obviously very important as they give direct unambiguous information about the structure of a defect.

1e. Hyperfine interaction

It is much easier to deal with hyperfine interactions on a quantitative basis. The reason is that this interaction arises from dipole-dipole coupling between the electronic and nuclear moments $\vec{\mu}_e$ and $\vec{\mu}_n$ and that an expression for this interaction is readily available. The dipole-dipole energy for separation $\vec{r}$ between the moments is given by:

$$H = \frac{\mu_o}{4\pi} \left\{ \frac{\vec{\mu}_e \cdot \vec{\mu}_n}{r^3} - 3 \frac{(\vec{\mu}_e \cdot \vec{r})(\vec{\mu}_n \cdot \vec{r})}{r^5} \right\} , \qquad (6)$$

$$H = - \frac{\mu_o}{4\pi} g_e \mu_B g_N \mu_N \left\{ \frac{\vec{J} . \vec{I}}{r^3} - 3 \frac{(\vec{J} . \vec{r})(\vec{I} . \vec{r})}{r^5} \right\} . \qquad (7)$$

The expression can be cast in the form $\vec{J}.\overleftrightarrow{A}.\vec{I}$, as given in the spin-Hamiltonian (equation 4). To evaluate the hyperfine tensor components $A_{\alpha\beta}$ the interaction must be averaged over the electron positions $\vec{r}$ with respect to the nucleus. With electron wave function ψ the $A_{\alpha\beta}$ $(\alpha, \beta = x,y,z)$ are found from:

$$A_{\alpha\beta} = \langle \psi | (3 r_\alpha r_\beta - r^2 \delta_{\alpha\beta}) / r^5 | \psi \rangle \quad . \qquad (8)$$

A flexible approximation to the electron wave function is provided by the method of linear combination of atomic orbitals (LCAO). In the case of silicon a logical choice of basic functions are the atomic 3s and 3p wave functions. In this expansion the defect electron wave function is given by:

$$\psi = \sum_i (\alpha_i \chi_{3s,i} + \beta_{ix} \chi_{3px,i} + \beta_{iy} \chi_{3py,i} + \beta_{iz} \chi_{3pz,i}) , \qquad (9)$$

where the index i runs over lattice sites around the defect on which the atomic orbitals are centered. For semiconductors other than silicon, or when impurities are present, the appropriate atomic valence orbitals must be included in the expansion. For deep level defects the electron is quite strongly localized near the defect center. One thus expects large wave function coefficients for atoms on the defect site and for nearest neighbour positions, and generally decreasing values of the α's and β's for sites of increasing separation. By substitution of ψ

from equation (9) into equation (8) a relation is established between the wave function coefficients and the hyperfine constants. The hyperfine interaction with a magnetic nucleus on site i results primarily from the occupation of atomic orbitals centered on this same site. Using expansion (9) the isotropic part of the interaction, arising from the spherically symmetric s-part in the wave function, is separated from the axial part due to the atomic p-functions. Non-axial terms are outside the scope of a treatment based on an expansion with s- and p-orbitals only. A specific problem arises with the s-type orbital, since the integral has a singularity at the site of the nucleus, r = 0. Proper solution gives the result:

$$a_i = A_{xx,i} = A_{yy,i} = A_{zz,i} = \frac{8\pi}{3} \cdot \frac{\mu_o}{4\pi}\, g_e \mu_B g_N \mu_N\, \alpha_i^2 |\chi_{3s}(0)|^2$$

$$A_{xy,i} = A_{yz,i} = A_{zx,i} = 0 \qquad (10)$$

Having substituted p-functions into equation (8) their angular variables are easily integrated. For the axial part of the interaction one then obtains the principal values:

$$b_i = -A_{xx,i} = -A_{yy,i} = \frac{1}{2}A_{zz,i} = \frac{2}{5} \cdot \frac{\mu_o}{4\pi}\, g_e \mu_B g_N \mu_N\, \beta_i^2 <1/r^3>_{3p}\,, \qquad (11)$$

with $\beta_i^2 = \beta_{ix}^2 + \beta_{iy}^2 + \beta_{iz}^2$. On its own principal axes the hyperfine tensor is:

$$\overleftrightarrow{A_i} = \begin{pmatrix} a_i - b_i & 0 & 0 \\ 0 & a_i - b_i & 0 \\ 0 & 0 & a_i + 2b_i \end{pmatrix} . \qquad (12)$$

For most elements the atomic parameters $|\chi(0)|^2$ and $<1/r^3>$ were calculated using Herman-Skillman wave functions and are available in tabulated form. For silicon $|\chi_{3s}(0)|^2 = 34.6 \times 10^{30}\ m^{-3}$ and $<1/r^3>_{3p} = 18.2 \times 10^{30}\ m^{-3}$ /31/.

1f. Magnetic resonance spectrometer

The block diagram of the EPR-ENDOR spectrometer which is in use in the authors research group at the University of Amsterdam, is shown in figure 6 /32/. Its main features are

- Operation in the K-band, with microwave frequencies near 23 GHz, wavelength about 1.3 cm. A high microwave frequency is preferred since this enhances sensitivity and resolving power.
- Superheterodyne scheme. Two klystrons, A and B in the diagram, produce microwave signals with a slightly different frequency. Klystron B is the local oscillator in the receiver system. The signals are mixed in the balanced mixer BM I and BM II to produce an intermediate fre-

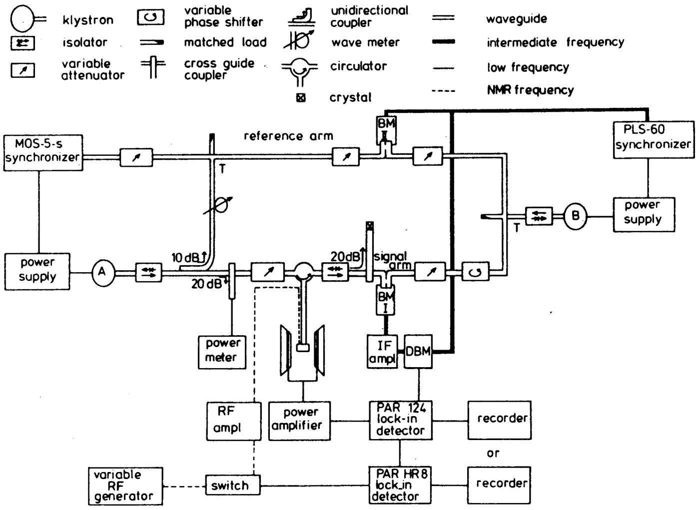

Figure 6. Block diagram of a superheterodyne EPR-ENDOR spectrometer. After Sieverts /32/.

quency IF. In our case this difference frequency equals 60 MHz. At these high frequencies the 1/f-noise of detection diodes is negligible.

- The resonance signal at the IF-stage, produced by BM I , is detected with respect to a reference IF signal, produced by BM II , in the double balanced mixer DBM. By adjusting the relative phase of the two signals, using the variable phase shifter, the spectrometer can be tuned to observe either the dispersive component χ' or the absorption component χ'' of the magnetic susceptibility $\chi = \chi' - i\chi''$.
- Samples are mounted in a reflection type microwave cavity. Depending on the sample shape a cylindrical cavity, resonating in the TE011 mode, or a rectangular cavity in the TE102 mode, is chosen.
- The microwave frequency of klystron A has to be adjusted carefully to the resonance frequency of the cavity. Therefore, the klystron frequencies are stabilized by comparing the signals to quartz crystal oscillators, fundamental frequency near 15 MHz, in the MOS-5-s and PLS-60 synchronizers.
- The magnetic field is stabilized and regulated using a Hall probe system. In search of a resonance the field can be linearly swept across a set field range in a set time.
- Accurate determination of the magnetic field strength B is made by a locked proton resonance system.
- Upon the linearly swept field an audio frequency modulated magnetic field is superposed. The resonance signal is detected phase sensitive with respect to this modulation.

- The magnetic field is rotatable around cavity and sample in the horizontal plane. Usually the samples are mounted with their $[0\bar{1}1]$ crystallographic axis vertically. In this way the magnetic field can be easily aligned parallel to the main crystal directions, which are $[100]$, $[111]$ and $[011]$.
- A cryogenic set-up allows operation with the sample at temperatures between 1.5 K and room temperature. The temperature stability is better than 0.1 K.
- For ENDOR measurements the required RF fields can be introduced in the cavity by a special coil insert. Alternatively, a cavity is available of which the silver plated cylindrical wall is machined in the form of a helical coil. The RF field is on-off modulated by an electronic switch. In the case of ENDOR experiments double phase sensitive detection is employed.
- Facilities to illuminate samples in the cavity with light, which can be monochromatic or polarized, are available. The light is channeled from outside the cryostat to the sample via a quartz rod insert or a hollow silver tube.
- Samples in the cavity can be subjected to uniaxial mechanical stress. Values up to 2 GPa have been realized. Forces are transmitted to the sample by a stainless steel stress rod insert.

2. Defects studied by magnetic resonance

2a. Vacancy and divacancy in silicon

Models of these intrinsic lattice defects, indicating pictorially in a simple manner the bond reconstruction, are shown in the figures 7 and 8. Deep levels in the band gap are associated with these defects.

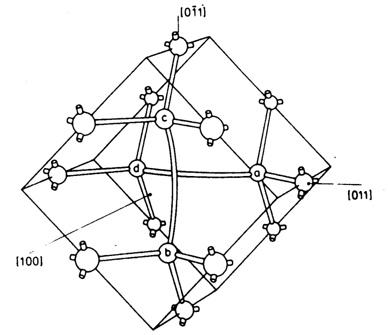

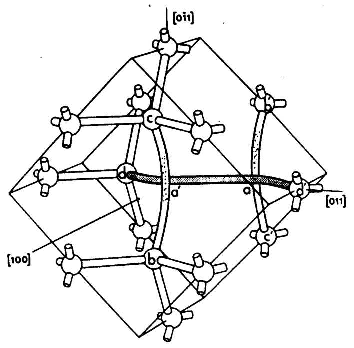

Figure 7. Model of the negative vacancy in the orientation labelled ad.

Figure 8. Model of the divacancy in the orientation labelled ad.

In both cases the defects have been observed in magnetic resonance in the positive and negative charge states /33-35/. The rotation patterns for $\vec{B}$ in the $(0\bar{1}1)$-plane are given in the figures 9 to 12. The positive

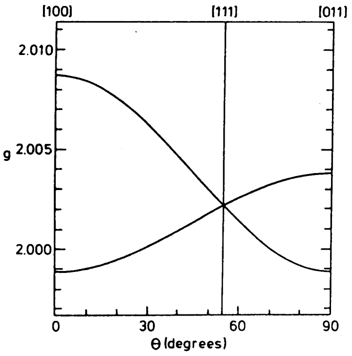

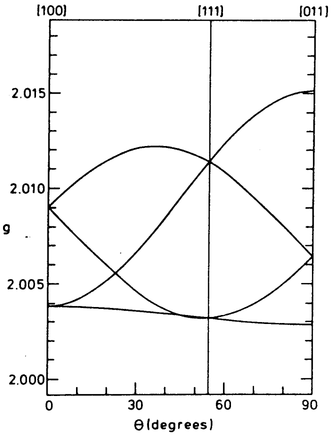

Figure 9. Angular dependence of the g-values of EPR spectrum Si-G1 corresponding to the positively charged vacancy Si:V^+.

Figure 10. Angular dependence of the g-values of EPR spectrum Si-G2 corresponding to the negatively charged vacancy Si:V^-.

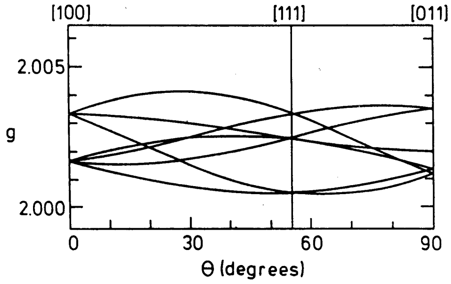

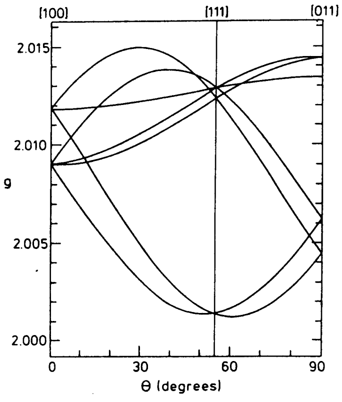

Figure 11. Angular dependence of the g-values of EPR spectrum Si-G6 corresponding to the positively charged divacancy Si:V_2^+.

Figure 12. Angular dependence of the g-values of EPR spectrum Si-G7 corresponding to the negatively charged divacancy Si:V_2^-.

vacancy V^+ has tetragonal symmetry, pointgroup $\bar{4}2m$. In the negative charge state V^- the lower rhombic I symmetry, pointgroup 2mm, is assumed by the defect. The divacancy has monoclinic I, pointgroup 2/m, symmetry in both charge states V_2^+ and V_2^-. Figure 13 illustrates the description

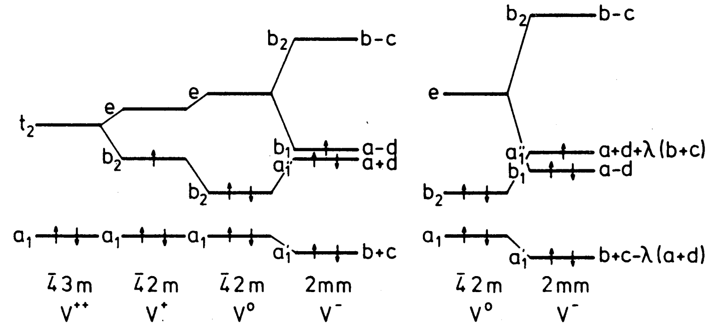

(a) (b)

Figure 13. (a) LCAO level scheme of the vacancy in its various charge states. (b) A revised scheme in which the b_1-level lies below the a_1''-level.

of the electronic structure of the vacancy in terms of a one-electron LCAO model. An electron occupying an orbitally degenerate state gives rise to the Jahn-Teller instability. The defect will spontaneously distort to lower symmetry, thereby lifting the degeneracy. The resulting lowering of the energy is the driving force for the distortion. It occurs when adding an electron to V^{++}, converting the vacancy into V^+. In cubic $\bar{4}3m$ symmetry the added electron will occupy the triply degenerate t_2-level. Upon distortion to the tetragonal $\bar{4}2m$ symmetry the occupation of the b_2-orbital as indicated in figure 13 results in lower energy, creating this new stable configuration. A similar situation is again encountered when changing the charge state from V^0 to V^-. The doubly degenerate e-level in symmetry $\bar{4}2m$ will split into the b_1 and b_2 singlet states. The symmetry is further lowered to rhombic I, pointgroup 2mm. All of this is in agreement with the experimental observations. For the divacancy a similar analysis also leads to conclusions which are confirmed by the experiments.

Detailed measurements of the hyperfine interactions for the vacancy and divacancy have been made using ENDOR /36-38/. Since for these intrinsic lattice defects no impurities are involved, the hyperfine interactions are with the ^{29}Si nuclei only. These have spin $I = \frac{1}{2}$ and the natural abundance of the magnetic isotope is 0.047. A more detailed discussion will be given here only for Si:V^-. Its EPR and ENDOR spectra are accurately described by $J = \frac{1}{2}$, $I_i = \frac{1}{2}$, and the spin-Hamiltonian:

$$H = \mu_B \vec{B}\cdot\overleftrightarrow{g}\cdot\vec{J} + \sum_i (\vec{J}\cdot\overleftrightarrow{A}_i\cdot\vec{I}_i - g_N\mu_N\vec{B}\cdot\vec{I}_i). \tag{13}$$

The summation i runs over atom sites around the vacancy, to each of which a specific strength of the hyperfine interaction $\overleftrightarrow{A}$ must be assigned. To analyse the hyperfine data it is again beneficial to exploit symmetry arguments fully. In the general case a ^{29}Si atom occupies a position with respect to the vacancy without particular qualities. By operating on this atom with the symmetry tranformations of V^-, contained in the group 2mm, three other sites are generated related to the original position by the symmetry. Together the 4 atoms constitute what is called a shell. The angular dependences of the ENDOR frequencies of all atoms in a shell form a typical pattern. In figure 14, representing the largest general class hyper-

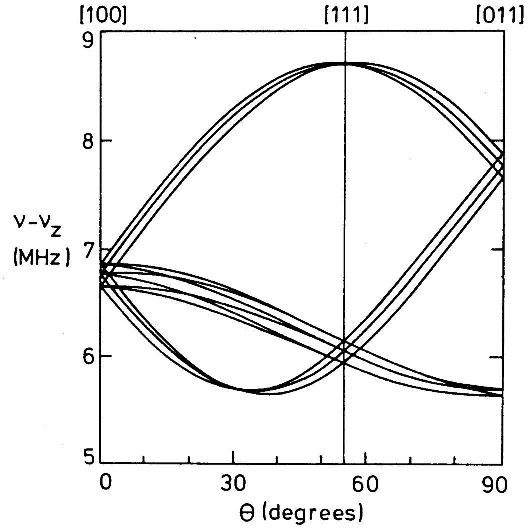

Figure 14. Angular dependence of the hyperfine interaction $\nu - \nu_z$ for the largest general class tensor. The interaction has nearly <111>-axial symmetry.

fine interaction, the difference of the ENDOR frequency ν and the ^{29}Si nuclear Zeeman frequency $\nu_z = g_N\mu_N B/h$ is plotted. However, the site occupied by the ^{29}Si nucleus may be on one of the mirrorplanes of the vacancy, or even be on both of them. In such particular cases the system (V^- + ^{29}Si nucleus) will be invariant under some or all of the operations in the pointgroup 2mm. This is reflected in a simplified structure of the hyperfine tensor. In the experiment it is revealed by symmetry required coincidences of the resonance frequencies. Characteristic simplifications in the rotational pattern will be observed. This is of great help in assigning the hyperfine tensors to specific shells of atoms.

In section 1e the conversion of the contact term a in the hyperfine interaction to the probability density of the defect electron was discussed. Results for the vacancy and divacancy are presented in the figures 15 and 16. In these pictures a monotonous decrease of the electron probability as a function of the distance to the defect is assumed /39/. The figures illustrate the electronic size of these deep level defects. The full lines in the figures are approximations by an expression $|\psi|^2 = A^2 \exp(-2r/r_o)$. The parameters A and r_o for best fits are given in table I. In particular in the case of V^- the wave function is far from spherical. The defect electron is predominantly localized in one of the mirrorplanes. Hyperfine studies thus provide detailed insight in the size and shape of defect electron clouds.

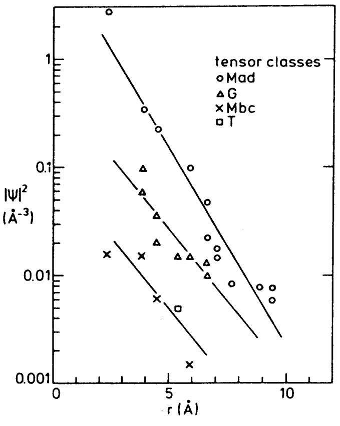

Figure 15. The probability density $|\psi|^2$ of the defect electron in the negative vacancy plotted against the distance r to the vacancy.

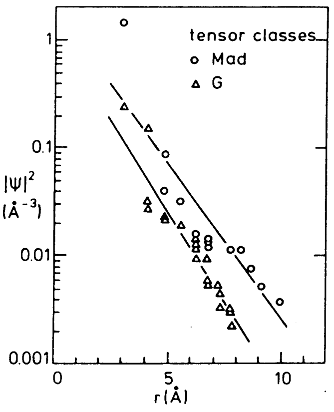

Figure 16. The probability density $|\psi|^2$ of the defect electron in the negative divacancy plotted against the distance r to the center of the divacancy.

Table I. Parameters of the empirical function $A^2 \exp(-2r/r_o)$, fitted to the values of $|\psi|^2$ of the vacancy and divacancy in silicon.

Defect	Type of shell	A^2 ($Å^{-3}$)	r_o (Å)
V^-	Mad	10	2.4
V^-	G	0.6	3.2
V^-	Mbc	0.1	3.0
V_2^-	M	2	3.0
V_2^-	G	1.1	2.6
V_2^+	M	7	1.9
V_2^+	G	4.3	1.9

A particular problem was encountered in the analysis of the ENDOR results for Si:V^-. On the basis of the generally adopted model the defect electron was expected to be in a b_1-type orbital. According to group theoretical classifications this is an orbital which is anti-symmetric when reflected in one of the vacancy's mirrorplanes. Consequently, the wave function is exactly zero in this mirrorplane, predicting a vanishing contact hyperfine term for the atoms in this plane. As is illustrated in figure 15 this is contradicting the ENDOR results. Though $|\psi|^2$ is small in mirrorplane bc, it is certainly not zero. A way out of this problem is suggested in the right part of figure 13. This revised level scheme is based on the assumption that the trigonal distortion of V^- is so large that the b_1-level moves below the a_1''-level. This results in an a_1-type ground state, allowing the contact terms as observed to exist. However, in the modified case the antibonding combination of the nearest neighbour orbitals a and d in state b_1 has lower energy than the bonding combination in state a_1''. This is not likely to be true. An alternative explanation can be found in the consideration of many-electron effects. Such more sophisticated treatments of defects are presently being developed /40/.

2b. Iron in silicon

Atoms of the 3d transition element series preferentially dissolve in silicon crystals on interstitial sites. Because of their high mobility these atoms are easily involved in defect interaction processes, such as impurity pair and complex formation, and in creating macroscopic precipitates. Since deep electronic levels in the silicon bandgap are associated with these defects, they affect carrier concentrations, lifetimes and trapping. Their presence in crystals, in concentrations up to about 10^{22} atoms per m^3, causes long term instabilities of the semiconductors and of the devices made in them. Studies of the electronic structure of transition metal impurities are therefore both of practical and fundamental interest.

A model to explain the electronic properties of the 3d transition metals in silicon was proposed by Ludwig and Woodbury /17,41/. The elements of the model are as follows:

- Transition metal atoms occupying substitutional sites transfer four electrons to the 4s and 4p orbitals to form sp^3 hybridized bonds with the four nearest neighbour silicon atoms. All remaining electrons are in the 3d shell. Interstitial atoms have all their valence electrons in the 3d shell.
- The cubic crystalline field partially lifts the five-fold orbital degeneracy of the 3d states into a doublet e and a triplet t_2 level. For substitutional atoms the doublet states are lower in energy than the triplet states. For interstitial impurity atoms the ordering is the reverse.
- The crystalline field is considered to be weak and therefore the doublet-triplet splitting is small. The electrons occupying these orbitals will obey Hunds rule of aligning spins. The maximum total spin consistent with the Pauli principle is obtained.

The application of the Ludwig-Woodbury model in analyzing the EPR spectra of iron in silicon is illustrated by three cases, in all of which only one iron atom is involved. The three cases considered are $Si:Fe_i^o$, $Si:Fe_i^+$ and $Si:Fe_s^+$, respectively.

For neutral interstitial iron, $Si:Fe_i^o$, which has the electronic configuration $(3d)^8$, the population of the t_2 and e levels by the eight electrons is shown in figure 17(a). The $^3A_2$ ground state is an orbital singlet, L' = 0, and has spin S = 1 as there are two unpaired electrons. The spin Hamiltonian appropriate for J = 1 is $H = \mu_B \vec{B}.\overleftrightarrow{g}.\vec{J} + \vec{J}.\overleftrightarrow{D}.\vec{J}$. However, because of the cubic symmetry of the tetrahedral interstitial site, the g-tensor reduces to a scalar g-value and the D-tensor vanishes. The level scheme of figure 18(a) applies. One EPR line is observed as the two transitions $m_J = -1 \leftrightarrow 0$ and $m_J = 0 \leftrightarrow +1$ coincide. The existence of two transitions is demonstrated by applying uniaxial stress to the crystal. In the lower symmetry of a strained crystal the D-tensor no longer vanishes and the two resonance fields will shift in opposite ways. The fine structure splitting by uniaxial compressive stress is shown in figure 18(b) /42,43/. The g-value g = 2.070 is close to g = 2, consistent with the quenching of the orbital momentum.

Positively charged interstitial iron, $Si:Fe_i^+$, has configuration $(3d)^7$ and the occupation of the levels is as shown in figure 17(b).

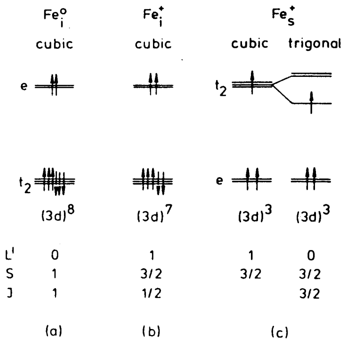

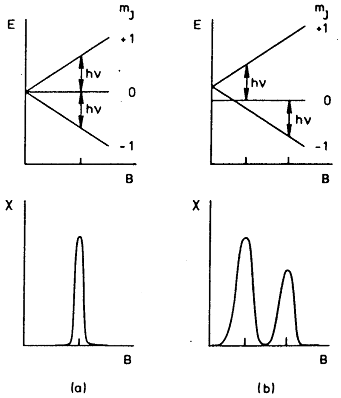

Figure 17. Electronic structure of interstitial and substitutional iron in silicon.

Figure 18. The fine structure splitting of the EPR spectrum of neutral interstitial iron in silicon induced by uniaxial stress. (a) Without stress, (b) with stress.

As there is one hole in the t_2 states an effective orbital angular momentum $L' = 1$ remains. The spin arising from 3 unpaired electrons is $S = 3/2$. In the ground state these momenta couple to a total $J = |L' - S| = 1/2$, in agreement with the EPR observation. With the orbital momentum a g-factor $g_{L'} = -3/2$ is associated. An adapted Landé formula gives the spectroscopic splitting factor as $g_{1/2} = 5/3\,g_s - 2/3\,g_{L'}$. For $g_s = 2$, $g_{L'} = -3/2$ the formula predicts $g_{1/2} = 13/3$; for $g_{L'} = 0$ one expects $g_{1/2} = 10/3$. The experimental result, an isotropic $g = 3.524$, is between these limits, but closest to the latter value. This is understood as a manifestation of the dynamic Jahn-Teller effect /44/. The orbitally degenerate ground state is Jahn-Teller instable. The effect is, however, small and the distortion rapidly moves from one direction into another. In the magnetic resonance experiment the average cubic symmetry is reflected in the isotropic g-value. The intricate mixing of atomic and electronic motion necessitates the use of vibronic wave functions. A consequent reduction of the matrix elements between spin states is known as the Ham effect. For Si:Fe$_i^+$ the orbital contribution to the g-factor is reduced from $g_{L'} = -3/2$ to about $g_{L'} = -0.3$.

A recently reported EPR spectrum labelled Si-NL19 possibly corresponds to substitutional iron in the positive charge state /45/. The spectrum is observed to strong intensity in iron-doped silicon after irradiation with energetic electrons. The vacancies produced in the irradiation may combine with interstitial iron atoms to form the substitutional impurity. Figure 7(c) illustrates the Ludwig-Woodbury model for Si:Fe_s^+. The electronic configuration $(3d)^3$ gives $S = 3/2$. One electron occupies the t_2 states, leading to $L' = 1$ and a triplet $^4T_2$ ground state. A static trigonal distortion may occur, lifting the degeneracy and quenching the orbital momentum completely. These predictions of the model are consistent with the analysis of spectrum Si-NL19. The angular variation for $\vec{B}$ in the $(0\bar{1}1)$-plane is shown in figure 19. All six transitions between the

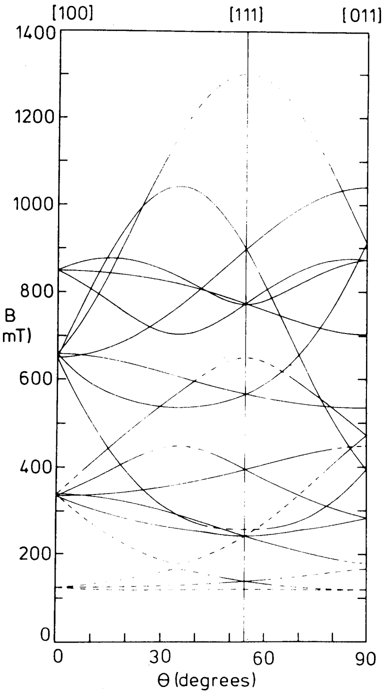

Figure 19. Rotation patterns of the resonance fields of spectrum Si-NL19 identified with positive substitutional iron in silicon.

four magnetic sublevels of spin $J = 3/2$ are observed. The patterns correspond to trigonal defect symmetry. The principal values of the g-tensor are $g_{/\!/} = 2.1163$ and $g_{\perp} = 2.0935$. The deviation from $g = 2$ by about +0.10 is comparable to that for Si:Fe_i^0. This is consistent with equation (5) assuming that the electronic structure of d shell electrons of iron atoms on substitutional and interstitial sites in silicon is rather similar.

2c. Nitrogen in diamond

Substitutional nitrogen atoms distributed as isolated centers are the predominant impurity in diamond crystals classified as type Ib. Though the atomic configuration of these centers is alike the column V impurities in the elemental semiconductors silicon and germanium, the electronic structure of the system C:N is entirely different. Deep donor levels in the bandgap of diamond, at about 2 eV below the conduction band, are associated with the nitrogen impurities. The atomic model of the defect is shown in figure 20; the electronic structure is illustrated by figure 21. Since the partly filled level is an orbital singlet a_1 stable cubic symmetry may be expected for the defect. This, however, does not correspond to the actually observed situation. An instability for trigonal distortion arises from interlevel coupling between the a_1 and t_2 states. This is also indicated in the figures 20 and 21.

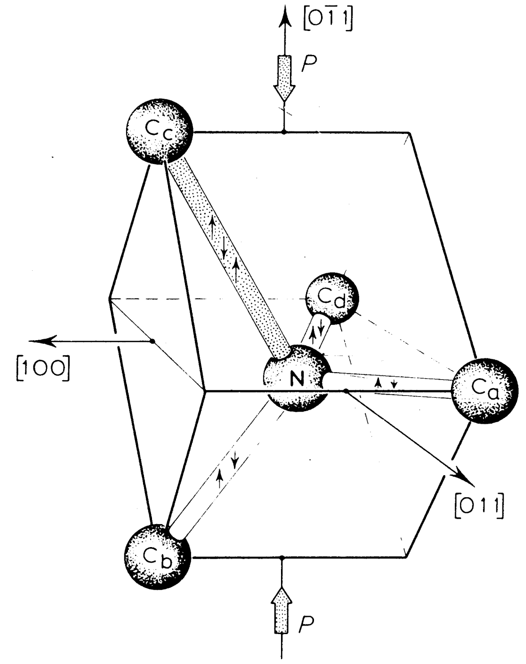

Figure 20. Model of substitutional nitrogen in diamond in the orientation labelled c. Also indicated is uniaxial compressive stress $\vec{P}$ along $[0\bar{1}1]$.

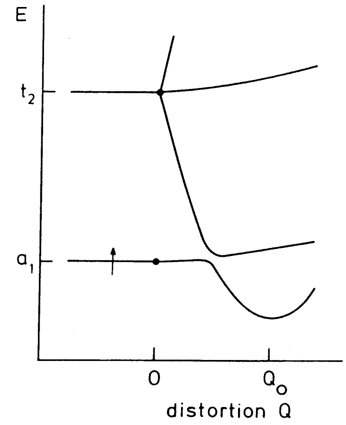

Figure 21. Effect of trigonal distortion Q on the energy levels of substitutional nitrogen in diamond.

The neutral donors are observable in electron paramagnetic resonance /46,47/. The angular dependence of the resonances in this C-P1 spectrum is given in figure 22. It can be analyzed using the spin-Hamiltonian

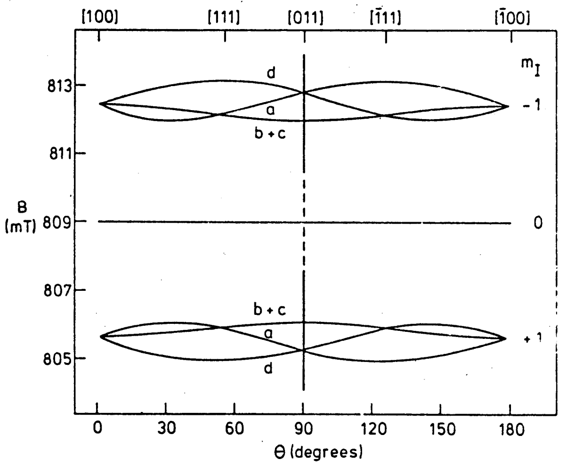

Figure 22. Resonance fields for the EPR spectrum of neutral substitutional nitrogen in diamond. Curves are labelled with the corresponding defect orientations. The vertical line at $\theta = 90^o$ indicates the magnetic field scan for the spectra shown in figure 24.

$$\mathcal{H} = g\mu_B\vec{B}.\vec{J} + \vec{J}.\overleftrightarrow{A}.\vec{I}, \tag{14}$$

with J = 1/2. A hyperfine interaction term is included since the ^{14}N atoms, abundance 99.63%, have nuclear spin I = 1. The energy levels E are given by

$$E = g\mu_B Bm_J + A(\theta)m_Jm_I, \tag{15}$$

with $m_J = \pm 1/2$, $m_I = -1, 0, +1$, and θ specifying the direction of the magnetic field. The resonance condition is

$$h\nu = g\mu_B B + A(\theta)m_I. \tag{16}$$

In principle, the trigonal symmetry of the defect should be reflected in an angular dependence of the g-factor, as in figure 4. However, for the light atoms carbon and nitrogen, forming the present system, the spin-orbit coupling constant is very small. As a result the g-value, g = 2.0024, deviates only slightly from the free electron value g = 2.0023, as predicted by equation (5). The angular variation due to g, which should be observable in the $m_I = 0$ resonance, is not resolved. Nevertheless, the true trigonal symmetry of the center is clearly demonstrated by the angular dependence of the ^{14}N hyperfine interaction A(θ) observable in the $m_I = \pm 1$ resonances.

Information on the distortion of the nitrogen centers can be obtained from experiments where uniaxial stress is applied to the crystal /48/. In a strained crystal the equivalence in energy of the nitrogen orientations is destroyed. As an example, figure 23 illustrates

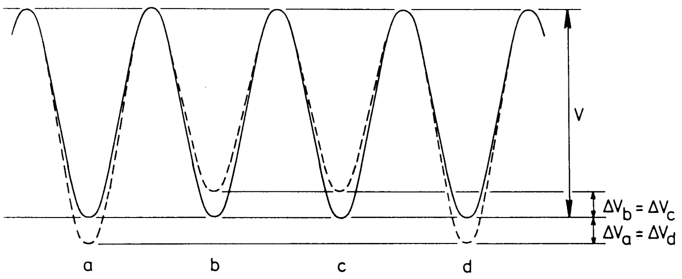

Figure 23. Schematic representation of the potential barriers separating the nitrogen center in the orientations a, b, c and d. Without stress (full curve) and with stress $\vec{P}//[0\bar{1}1]$ (dashed curve).

that $[0\bar{1}1]$ uniaxial compressive stress increases the energy of the $b = [11\bar{1}]$ and $c = [1\bar{1}1]$ orientations, but lowers the energy of the $a = [\bar{1}11]$ and $d = [\bar{1}\bar{1}\bar{1}]$ orientations. Since reorientations of the nitrogen centers are possible, an equilibrium will be established in which more nitrogen atoms will populate the a and d orientations, and fewer the b and c orientations. This phenomenon of stress induced ordering is directly observable in the EPR spectrum. Figure 24 illustrates that without stress the intensities of the resonances corresponding to pairs of nitrogen orientations, a+d versus b+c, are essentially equal. With stress applied the induced ordering is demonstrated by the increased intensity of the energetically favoured orientations a and d, and the accompanying loss of signal height for the higher energy orientations b and c.

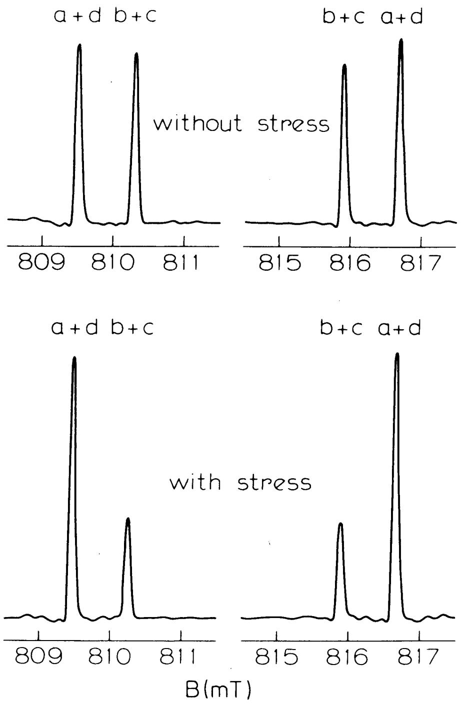

Figure 24. EPR spectrum of neutral substitutional nitrogen in diamond for $\vec{B}//[011]$, measured at the temperature T = 295 K, with and without compressive uniaxial stress of 1.97 GPa along the $[0\bar{1}1]$ direction. The central part of the spectrum, corresponding to $m_I = 0$, is omitted.

The degree of ordering increases with the stress as illustrated in figure 25. To analyze these data a deformation potential Ξ is introduced by $\Xi \equiv dE/de$. It represents the change of energy E per unit strain e.

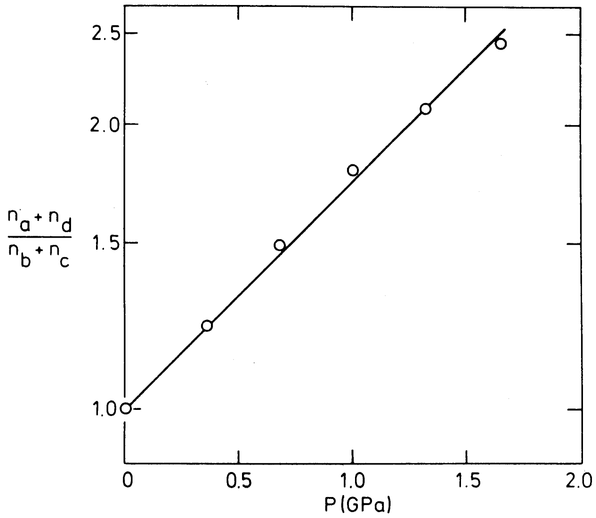

Figure 25. Ratio of the populations of the nitrogen orientations after alignment as a function of uniaxial stress $\vec{P}$ parallel to the $[0\bar{1}1]$ direction.

For the case of stress P along $[0\bar{1}1]$, as indicated in figure 20, the energy changes are $\Delta V_a = -\Delta V_b = -\Delta V_c = \Delta V_d = -\Xi S_{44}P/6$, where S_{44} is an elastic compliance constant of diamond. In equilibrium, when a Boltzmann distribution is established, the populations are given by $n_a = n_d$, $n_b = n_c$, and $\ln (n_a/n_b) = \Xi S_{44}P/3kT$. From the slope of the line in figure 25 the value $\Xi = -21$ eV follows. The deformation potential is a measure of the coupling between electron states and the lattice geometry. The large value of Ξ together with the size of the trigonal distortion of the nitrogen atom account for the deep position of the donor state. The donor electron in the deep level is primarily bound by the distortion, in contrast to the Coulomb binding of electrons in shallow donor states.

After removal of the stress any existing ordering will disappear by random reorientation processes /49/. This effect can be studied as a function of temperature. Figure 26 illustrates the anneal of stress induced ordering at two temperatures. Since the reorientation of the isolated nitrogen atoms obeys first order kinetics, the loss of excess population Δn will follow a time dependence

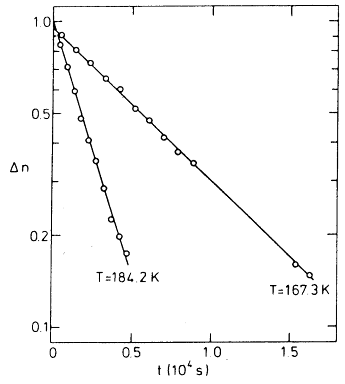

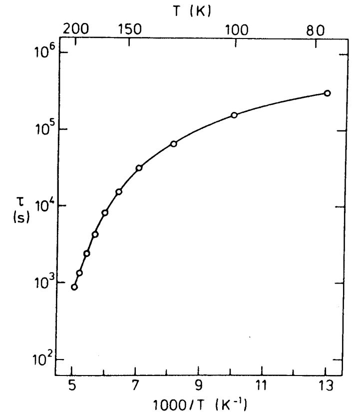

Figure 26. The anneal of stress induced ordering as a function of time t in isothermal anneal treatments at the temperatures T = 167.3 K and T = 184.2 K.

Figure 27. The relaxation time τ for anneal of stress induced ordering of substitutional nitrogen in diamond as a function of temperature T.

$$\Delta n = n(t) - n(\infty) = \{n(0) - n(\infty)\}.\exp(-t/\tau). \qquad (17)$$

It is characterized by a time constant τ which can be determined from the slope of the straight line plots in figure 26. The temperature dependence of the reorientation time constant is given in figure 27. At high temperatures, around 200 K, the straight line part of the curve indicates an Arrhenius behaviour of the reorientation process:

$$\tau = \tau_0.\exp(V/kT). \qquad (18)$$

The potential V is determined to be 0.76 eV. It corresponds to the height of the potential barriers between separate distortions, as illustrated in a schematic manner in figure 23. At low temperatures, typically below 100 K, the temperature dependence of the reorientation rate is much lower. Under these conditions the main mechanism of reorientation is tunneling through the potential barriers.

2d. Antisite defects in III-V compounds

An antisite defect is formed when a single atom occupies a regular position of the sublattice of the other chemical constituent in a binary compound. Anion and cation antisite centers can thus be distinguished. Electron paramagnetic resonance has been detected for several antisite centers in III-V compound semiconductors.

The first firm evidence by EPR was established for the P_{Ga} center in GaP /21,50-52/. The atomic model of this center is shown in figure 28. The antisite phosphorus atom is a double donor. Both in the neutral and doubly ionized states the center is diamagnetic. The EPR studies are made in the singly ionized state P_{Ga}^{+}. Interaction of the unpaired electron spin with the nuclear spins I = 1/2 of the phosphorus atoms on the central antisite position and on the four equivalent ligand sites was resolved in the EPR spectrum. The spectrum for $\overleftrightarrow{B}$ // <100> is given in figure 29. The hyperfine interaction with the antisite P atom causes a twofold splitting of the spectrum into components with equal intensities. The four ligand P atoms give rise to a further hyperfine splitting into 2^4 components, which for $\overleftrightarrow{B}$ // <100> coincide in such a way as to generate a five line spectrum with intensity ratios 1:4:6:4:1. The hyperfine structure in the EPR spectrum reflects the atomic structure of the antisite center in a very characteristic way.

The spin-Hamiltonian

$$H = \mu_B \vec{B}.\overleftrightarrow{g}.\vec{J} + \vec{J}.\overleftrightarrow{A}_c.\vec{I} + \sum_{i=1}^{4} \vec{J}.\overleftrightarrow{A}_{Li}.\vec{I}_i \qquad (18)$$

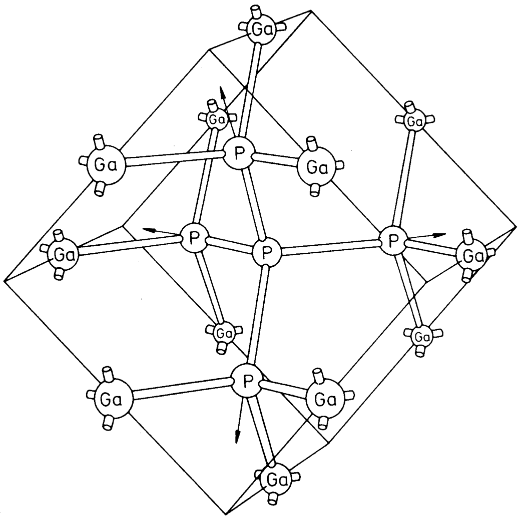

Figure 28. Atomic model of the P_{Ga} antisite center in GaP.

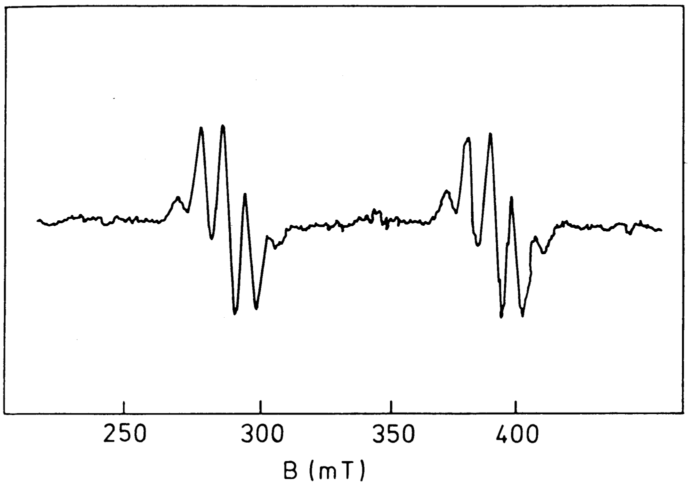

Figure 29. EPR spectrum of the P_{Ga} antisite defect in GaP for $\vec{B}//<100>$. After Kaufmann and Schneider /23/.

takes these interactions into account. The g-value, g = 2.007, is isotropic. Also, the hyperfine interaction $\overleftrightarrow{A}_c$ with the central phosphorus atom is isotropic. Its value is a_c/h = 2896 MHz. Apparently, the center does not undergo a symmetry lowering distortion. In accordance with the defect model the hyperfine interactions $\overleftrightarrow{A}_{Li}$ with the ligand phosphorus atoms have a <111> axial symmetry. The principal values of these interaction tensors are $A_{//}/h$ = 314 MHz and $A_{\perp}/h$ = 179 MHz. Using the identities from equation (12) $A_{//} = a + 2b$ and $A_{\perp} = a - b$, one finds a_L/h = 224 MHz and b_L/h = 45 MHz. To interpret these data in more physical terms an LCAO wave function, similar to (9),

$$\psi = \alpha_c \chi_{3s,c} + \sum_{i=1}^{4} (\alpha_{Li}\chi_{3s,Li} + \beta_{Li}\chi_{3p,Li})$$

is constructed. With the atomic parameters applicable to phosphorus, $\chi^2_{3s}(0) = 41.6 \times 10^{24}$ cm^{-3} and $<1/r^3>_{3p} = 24.2 \times 10^{24}$ cm^{-3}, the wave function coefficients become $\alpha_c = 0.26$, $\alpha_{Li} = 0.02$ and $\beta_{Li} = 0.145$. These results imply that the wave function is concentrated for 26 % on the central atom and for 66 % on the four ligand atoms together. Since 92 % of the wave function is found in the region of the PP_4 cluster, it is concluded that the defect electron is strongly localized. This is consistent with the deep level character of the antisite defect /51/. The hybrid orbitals on the ligand atoms pointing towards the central atom are strongly p-type. From the figures given above it follows that these orbitals are 12% s-type only and 88% p-type, which is more than corresponding to normal sp^3 hybridization. Consequently the bonds of the ligand phosphorus atoms with their three other neighbours, that is the three gallium atoms, will be less p-type than sp^3. These bonds are more planar than in normal tetrahedral geometry. This indicates a distortion in which the ligand atoms move away from the central site. Such a breathing mode relaxation does not affect the cubic symmetry.

EPR observations of the As_{Ga} antisite center in GaAs have also been reported /53-55/.

References

/1/. G.Lancaster
Electron Spin Resonance in Semiconductors
(Hilger and Watts, 1966).

/2/. G.D.Watkins
Point Defects in Solids. Volume 2. Semiconductors and Molecular Crystals. J.H.Crawford and L.M.Slifkin, editors (Plenum Press, 1975), p.333.

/3/. G.Feher
Phys.Rev. 114, 1219 (1959).

/4/. D.Haneman
Phys.Rev. 170, 705 (1968).

/5/. D.Haneman, M.F.Chung and A.Taloni
Phys.Rev. 170, 719 (1968).

/6/. H.Alexander, C.Kisielowski-Kemmerich and E.R.Weber
Physica 116 B, 583 (1983).

/7/. D.Jérome and J.M.Winter
Phys.Rev. 134, A1001 (1964).

/8/. S.Maekawa and N.Kinoshita
J.Phys.Soc.Japan 20, 1447 (1965).

/9/. J.W.Corbett, R.L.Kleinhenz and N.D.Wilsey
Materials Research Society Symposia Proceedings. Volume 2. Defects in Semiconductors, J.Narayan and T.Y.Tan, editors (North-Holland Publishing Company, 1981), p.1.

/10/. J.W.Corbett and J.C.Bourgoin
Point Defects in Solids. Volume 2. Semiconductors and Molecular Crystals. J.H.Crawford and L.M.Slifkin, editors (Plenum Press, 1975), p.1.

/11/. W.Kohn
Solid State Physics. Volume 5. F.Seitz and D.Turnbull, editors (Academic Press, 1957), p.258.

/12/. D.K.Wilson and G.Feher
Phys.Rev. 124, 1068 (1961).

/13/. D.K.Wilson
Phys.Rev. 134, A265 (1964).

/14/. E.B.Hale and R.L.Mieher
Phys.Rev. 184, 739 (1969).

/15/. H.Neubrand
Phys.Stat.Sol.(b) 86, 269 (1978).

/16/. G.W.Ludwig
Phys.Rev. 137, A1520 (1965).

/17/. K.L.Brower
Phys.Rev.Letters 44, 1627 (1980).

/18/. K.L.Brower
Materials Research Society Symposia Proceedings.
Volume 3. Nuclear and Electron Resonance Spectroscopies
Applied to Materials Science. E.N.Kaufmann and G.K.Shenoy,
editors (North-Holland Publishing Company, 1981), p.71.

/19/. G.W.Ludwig and H.H.Woodbury
Solid State Physics, Volume 13. F.Seitz and D.Turnbull,
editors (Academic Press, 1962), p.223.

/20/. E.R.Weber
Appl.Phys. A 30, 1 (1983).

/21/. G.D.Watkins and J.W.Corbett
Phys.Rev. 121, 1001 (1961).

/22/. G.D.Watkins and J.W.Corbett
Phys.Rev. 134, A1359 (1964).

/23/. U.Kaufmann and J.Schneider
Festkörperprobleme (Advances in Solid State Physics),
Volume XX, J.Treusch, editor (Vieweg, 1980), p.87.

/24/. G.E.Pake and T.L.Estle
The Physical Principles of Electron Paramagnetic Resonance
(Benjamin, 1973).

/25/. W.Low
Solid State Physics. Supplement 2. Paramagnetic Resonance in
Solids (Academic Press, 1960).

/26/. C.P.Slichter
Principles of Magnetic Resonance (Harper and Row, 1963).

/27/. C.A.J.Ammerlaan
Atomic Energy Review 12, 743 (1974).

/28/. M.H.L.Pryce
Proc.Phys.Soc. 63, 25 (1950).

/29/. A.Abragam and M.H.L.Pryce
Proc.Roy.Soc. A 205, 135 (1951).

/30/. B.Bleaney and K.W.H.Stevens
Reports on Progress in Physics 16, 108 (1953).

/31/. J.R.Morton and K.F.Preston
J.Magnetic Resonance 30, 577 (1978).
/32/. E.G.Sieverts
thesis, University of Amsterdam (1978).
/33/. G.D.Watkins
J.Phys.Soc.Japan 18, 22 (1963).
/34/. G.D.Watkins
Radiation Damage in Semiconductors (Dunod, 1965), p.97.
/35/. G.D.Watkins and J.W.Corbett
Phys.Rev. 138, A543 (1965).
/36/. J.G. de Wit, E.G.Sieverts and C.A.J.Ammerlaan
Phys.Rev.B 14, 3494 (1976).
/37/. E.G.Sieverts, S.H.Muller and C.A.J.Ammerlaan
Phys.Rev. B 18, 6834 (1978).
/38/. M.Sprenger, S.H.Muller and C.A.J.Ammerlaan
Physica 116 B , 224 (1983).
/39/. E.G.Sieverts
J.Phys.C: Solid State Phys. 14, 2217 (1981).
/40/. M.Lannoo
Phys.Rev., to be published.
/41/. G.W.Ludwig and H.H.Woodbury
Phys.Rev.Letters 5, 98 (1960).
/42/. H.H.Woodbury and G.W.Ludwig
Phys.Rev. 117, 102 (1960).
/43/. M.Berke, E.Weber, H.Alexander, H.Luft and B.Elschner
Solid State Communications 20, 881 (1976).
/44/. F.S.Ham
Electron Paramagnetic Resonance. S.Geschwind, editor
(Plenum Press, 1972),p.1.
/45/. S.H.Muller, G.M.Tuynman, E.G.Sieverts and C.A.J.Ammerlaan
Phys.Rev. B 25, 25 (1982).
/46/. W.V.Smith, P.P.Sorokin, I.L.Gelles and G.J.Lasher
Phys.Rev. 115, 1546 (1959).
/47/. J.H.N.Loubser and J.A. van Wijk
Reports on Progress in Physics 41, 1201 (1978).
/48/. C.A.J.Ammerlaan and E.A.Burgemeister
Industrial Diamond Rev. 40, 128 (1980).
/49/. C.A.J.Ammerlaan and E.A.Burgemeister
Phys.Rev.Letters 47, 954 (1981).
/50/. U.Kaufmann, J.Schneider and A.Räuber
Applied Physics Letters 29, 312 (1976).
/51/. U.Kaufmann, J.Schneider, R.Wörner, T.A.Kennedy and N.D.Wilsey
J.Phys.C: Solid State Phys. 14, L951 (1981).

/52/. N.Killoran, B.C.Cavenett, M.Godlewski, T.A.Kennedy and N.D.Wilsey
Physica 116 B, 425 (1983).

/53/. R.J.Wagner, J.J.Krebs, G.H.Stauss and A.M.White
Solid State Communications 36, 15 (1980).

/54/. R.Wörner, U.Kaufmann and J.Schneider
Applied Physics Letters 40, 141 (1982).

/55/. E.R.Weber and J.Schneider
Physica 116 B, 398 (1983).